International Journal of Nanomedicine

Dovepress
open access to scientific and medical research

Open Access Full Text Article

ORIGINAL RESEARCH

Hybrid $FeWO_4$-Hyaluronic Acid Nanoparticles as a Targeted Nanotheranostic Agent for Multimodal Imaging-Guided Tumor Photothermal Therapy

Chunmei Yang[1,*], Xiaoling Che[1,*], Yu Zhang[2], Didi Gu[1], Guidong Dai[1], Jian Shu[1], Lu Yang[1]

[1]Department of Radiology, The Affiliated Hospital of Southwest Medical University, Nuclear Medicine and Molecular Imaging Key Laboratory of Sichuan Province, Luzhou, Sichuan Province, People's Republic of China; [2]Department of Radiology, The First People's Hospital of Yibin, Yibin, 644000, People's Republic of China

*These authors contributed equally to this work

Correspondence: Jian Shu; Lu Yang, Department of Radiology, The Affiliated Hospital of Southwest Medical University, Luzhou, Sichuan Province, People's Republic of China, Tel +86 0830-18980253083; +86 0830-2504762, Email shujiannc@163.com; yanglu@swmu.edu.cn

Background: Development of versatile nanoplatform still remains a great challenge due to multistep synthesis and complicated compositions. Therefore, it is significant to develop a facile method to synthesize a nanocomposite to achieve multimodal imaging and even imaging-guided cancer therapeutics.

Methods and Results: In our study, hyaluronic acid-functionalized iron (II) tungstate nanoparticles (HA-$FeWO_4$ NPs) were successfully synthesized as a versatile nanoplatform by a facile one-pot hydrothermal procedure. The formed multifunctional HA-$FeWO_4$ NPs were investigated via a series of characterization techniques, which demonstrated good biocompatibility, excellent dispersion, low cytotoxicity, active tumor-targeting ability and high photothermal efficiency. Furthermore, tumor was clearly visualized by HA-$FeWO_4$ NPs with multimodal imaging of infrared thermal imaging, magnetic resonance imaging, computed tomography imaging in 4T1 tumor bearing mice. More importantly, HA-$FeWO_4$ could achieve multimodal imaging-guided photothermal therapy of 4T1 tumors.

Conclusion: The constructed HA-$FeWO_4$ NPs have great potential as ideal nanotheranostic agents for multimodal imaging and even imaging-guided cancer theranostics in biological systems.

Keywords: theranostics, multimodal imaging, photothermal therapy, diagnostic imaging, nanomedicine

Introduction

Multimodal imaging integrated with two or more imaging modalities has significant impact on the medical detection and diagnosis of various diseases.[1–3] Imaging technologies such as near-infrared (NIR) imaging, computed tomography (CT) imaging, magnetic resonance imaging (MRI), and positron emission tomography (PET) have been widely studied and applied in various fields. Of these, CT can provide images with high spatial and density resolution, while MRI offers favourable soft tissue contrast. Therefore, dual-modality CT/MRI imaging with complementary properties is beneficial for improving the efficiency of diagnosis. The development of contrast agents with multimodal imaging ability is necessary for more accurate diagnosis since they have superior sensitivity and could distinguish lesion from normal tissues. More importantly, multimodal imaging is expected to reduce the dosages of contrast agents, hence reducing their toxicity and side effects.

Nowadays, clinically used contrast agents are mainly small molecular ones such as iodinated molecules and gadolinium chelates. Compared with small molecular contrast agents, nanomaterial is not so easily degraded by enzymes, and has advantages of strong signal, outstanding targeting ability, long half-life, and easy introduction of multifunctional groups. It's reported that many multimodal nano-contrast agents have been synthesised and applied in medical analysis

Received: 14 September 2023
Accepted: 20 December 2023
Published: 28 December 2023

in vivo, for instance, Au/PPY@Fe_3O_4,[4] PEGylated $NaHoF_4$,[5] Gd@Au PENPs,[6] $NaDyF_4$: 50%Lu@ Prussian blue[7] and FeBi NPs.[8] These nanoparticles have amazing imaging performance and great potential in multimodal imaging of different biological systems. However, as far as we know, there is still no appropriate multimodal imaging contrast agent used in clinical practice.

Metal tungstates are regard as important members of inorganic functional materials family with widely application in various fields, including microwave applications, photoluminescence, scintillator materials, optical fibers, catalysts, humidity sensors, magnetic material,[9–12] and biomedicine.[13,14] Tungstate nanomaterials, such as $FeWO_4$,[15] $MnWO_4$,[16] $BaWO_4$,[17] $ZnWO_4$,[18] Bi_2WO_6,[19] and $PbWO_4$,[20] have attracted much attention because of their unique properties, and great potential in clinical applications. Among the various metal tungstates, $FeWO_4$, as a p-type oxide semiconductor material, owns outstanding electronic and optical properties. Furthermore, the magnetic Fe^{2+} in $FeWO_4$ endows them with ferromagnetic properties, and the presence of tungsten (W, Z = 74) suggests that it could be used as a sensitive CT imaging contrast agent due to the high X-ray attenuation coefficient. Recently, nanomaterials based on $FeWO_4$ have been developed using various methods and applied in the fields of efficient visible-light photocatalysis, electron transport, humidity sensor, wastewater treatment and the construction of cost-efficient and environmentally benign fuel cells.[21–24] However, the multimodal imaging ability of $FeWO_4$ was rarely mentioned due to batch-to-batch variation, nanoparticle aggregation and uncertain targeting ability.[25] Therefore, it is significant but challenging to prepare high-performance $FeWO_4$ based nanomaterial for multimodal imaging.

Of note, ideal nanomaterials not only have sensitive multimodal imaging capability but also own excellent targeting ability. Hyaluronic acid (HA), a specific ligand for cell surface overexpressing CD44 HA receptors,[26] which is over-expressed in some malignant tumors, such as breast cancer.[27–29] Therefore, the introduction of HA provides a theoretical basis for ligand guided therapy of breast cancer.[30,31] Currently, researchers have developed various CD44-targeted nanoprobes for disease imaging.[21,32–35] These studies prove the potential of HA in developing multifunctional diagnostic or theranostic nanoplatform for tumor imaging and treatment, which inspire us to hybridize HA with $FeWO_4$ based nanomaterial for the preparation of nanotheranostic agent.

To date, photothermal therapy (PTT), which converts photon energy to heat energy and kills cancer cells by a hyperthermia process, has attracted great attention in cancer treatment due to its advantages of simple operation, minimal invasiveness, and target selectivity.[36,37] PTT is a highly effective and non-invasive technique for cancer therapy.[38,39] It's reported that a variety of nanomaterials with intense near-infrared absorption, such as noble metal nanoparticles (gold and silver),[40,41] carbon-based nanomaterials (graphene), transition metal chalcogenides (Cu_xS_y, MoS_2, WS_2 and Bi_2S_3) or oxides nanoparticles (WO_{3-x}, MoO_{3-x} and RuO_2•xH_2O) have been used as photothermal agents to construct theranostic platform of cancer.[42–45] Very recently, we developed a folic acid receptor-targeted $CuFeSe_2$ nanoprobe, which could achieve MRI/CT dual-modality imaging of tumors in vivo and had a great potential as a photothermal therapeutic agent for cancer.[46] Among these reported nanomaterials, W has high X-ray attenuation ability and W-based nanomaterials have outstanding photothermal conversion efficiency, and thus WS_2 nanosheets and WO_{3-x} nanorods have been utilized as CT imaging/photothermal agents. However, few relevant investigations of $FeWO_4$-based nanomaterials have been reported in the field of in vivo multimodal imaging-guided photothermal therapy of cancer to date.

Materials and Methods

Chemicals and Materials

$FeSO_4$•$7H_2O$, and Na_2WO_4•$2H_2O$ were purchased from Acros (Beijing, China). Hyaluronic acid (HA, sodium salt, Mw ≈ 240 KD) was obtained from Beijing Mreda Technology Co., Ltd. (Beijing, China). Dulbecco's minimum essential medium (DMEM), Roswell Park Memorial Institute-1640 (RPMI-1640) medium, and fetal bovine serum (FBS) were purchased from GIBCO (Thermo Fisher Scientific, Waltham, MA, USA). Penicillin-streptomycin solution and Trypsin-EDTA solution were purchased from Beyotime Biotechnology Co., Ltd. (Shanghai, China). 4T1 and MCF-10A cells were provided by Procell Life Science & Technology Co., Ltd. (Wuhan, China).

Synthesis of HA-$FeWO_4$ Nanoparticles

The HA-$FeWO_4$ nanoparticles were prepared by a modified literature protocol.[16] Specifically, 278 mg $FeSO_4$•$7H_2O$ and 960 mg of HA were added in 60 mL of DI water under vigorous stirring. Then, a solution of 289 mg of Na_2WO_4•$2H_2O$ in 10 mL of DI water was slowly added to the mixture solution. After further mixing for 4 h, the obtained colloidal solution was then transferred into a 100-mL Teflon-lined stainless steel autoclave and sealed and heated at 140°C for 8 h. After cooling to room temperature, the HA-$FeWO_4$ nanoparticles were collected by centrifugation and washed with DI water for three times. The product of HA-$FeWO_4$ nanoparticles were freeze dried for later use. The synthesis process is shown in Scheme 1.

Characterization

Transmission electron microscope (JEM 2100F, JEOL, Japan) was used to detect the morphology of HA-$FeWO_4$ NPs at 200 kV and the crystal structure of HA-$FeWO_4$ was analysed using X-ray diffraction (D8, Bruker, Germany) with Co Kα radiation at 40 kV and 40 mA. The scan range (2θ) was 10–80°, scan rate was 6°/min. W and Fe contents in the HA-$FeWO_4$ were detected using ICP-OES730 (Agilent, USA). Different chemical bonds in HA-$FeWO_4$ and HA were measured on a FTIR (Shimadzu, Japan).

The Colloidal Stability of HA-$FeWO_4$ Nanoparticles

To evaluate the colloidal stability of HA-$FeWO_4$ NPs, HA-$FeWO_4$ NPs was dissolved in different media, such as normal saline, PBS, DMEM and RPMI-1640 for 14 days at 37°C.

Relaxivity and Hounsfield Unit (HU) Value Measurement

Different concentrations of Fe dispersions (0, 1.75, 3.5, 7, 14 mM) were performed to measure the longitudinal/transverse relaxivity time (T1/T2). After line-fitting the 1/T1 or 1/T2 versus Fe concentration, their longitudinal and transverse (r_1/r_2) were obtained. The HA-$FeWO_4$ solutions with different concentrations of W (0, 2.5, 5, 10, 20 mM) were also prepared to evaluate the potential of nanomaterial in CT imaging. CT and MRI of HA-$FeWO_4$ solutions were carried out on spectral CT (IQon, Philips, Holland) and 3.0 T MRI (Siemens, German), respectively. As a control, CT scanning of iohexol in vitro was also performed. The parameters of MRI scan were echo time (TE) 68 ms, repetition time (TR) 5290 ms, slice thickness 1 mm, matrix 256 × 256, field of view 180 mm, number of excitations 2. The parameters of CT scan were tube current 100 mAs, tube voltage 120 kV, matrix 512 × 512, slice thickness 0.8 mm, and field of view (FOV) 150 mm.

Cell Culture and Cytotoxicity Assessment

4T1 and MCF-10A cells were cultured in RPMI-1640 and DMEM, respectively, at 37°C and 5% CO_2 conditions. The cell cytotoxicity was evaluated using the CCK-8 test. 4T1 and MCF-10A cells were seeded into 96-well microplates at a density of 5000 cells per well and then incubated for 24 h at 37°C and 5% CO_2. Next, HA-$FeWO_4$ at various concentrations were added separately into wells and cultured for 24 h. Cell viability was calculated by measuring absorbance at 450 nm.

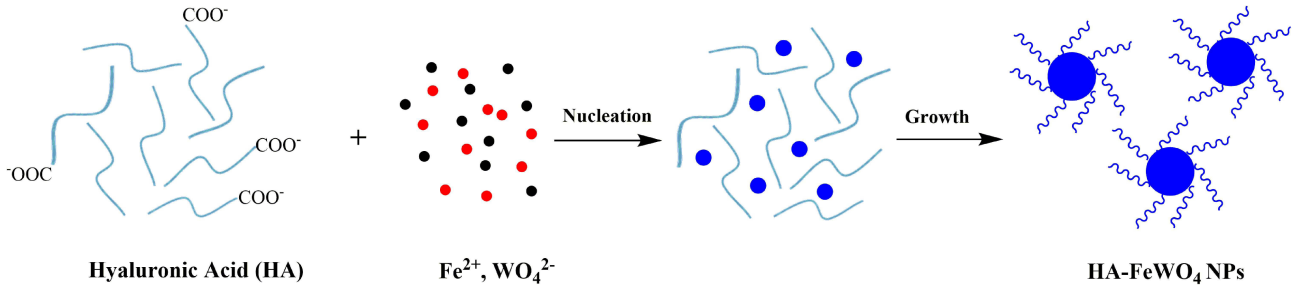

Scheme 1 Schematic illustration of the growth process for HA-$FeWO_4$ nanoparticles.

Vitro Targeted Assessment

First, 4T1 cells were seeded in 6-well plates at 1.5×10^4 cells/well density. Cells were then treated with different concentrations of HA-$FeWO_4$ (0, 100, 200, 400 μg/mL). As a control, the other group cells was first treated with HA (4 mg/mL) for 4 h. Afterward, cells were washed with PBS (pH 7.4) and then different concentrations of HA-$FeWO_4$ (0, 100, 200, 400 μg/mL) were also added. After incubation for 4 h, the cells were washed with PBS (pH 7.4) three times. Subsequently, all cells were digested by pancreatin for MRI. MRI was performed using a Siemens Prisma 3.0T MR system. T2 weighted imaging (T2WI) was obtained with 1 mm slice thickness, 5290/68 ms TR/TE, 180 mm FOV, 256×256 matrix and 2 NEXs. Finally, Fe content in cells was measured by ICP-OES.

Hemolysis Assay

All animal experiments were performed according to the guidelines and protocols approved by the Institutional Animal Care and Use Committee of Southwest Medical University (accreditation number: 20211122–026). First, fresh mouse blood was collected from Sprague Dawley (SD) female rats and centrifuged at 1000 rpm to get the red blood cells (RBCs). Next, RBCs for the following hemolysis test were obtained on the basis of the previous study.[47] Detailedly, the RBCs were isolated from serum by centrifugation and then purified by washing with by saline three times. Then, the diluted RBCs (1.5 mL) was mixed with different concentrations of HA-$FeWO_4$ solutions (50, 100, 200 μg/mL, 150 μL) with saline as the solvent and cultured at 37°C for 4 h. Next, the mixtures were centrifuged to discard the cells. The absorbance of the supernatant at 541 nm was measured by UV spectrophotometer (UV3600, Shimadzu, Japan). Ultrapure water was used as positive control and normal saline as negative control, respectively.

Toxicity Assessment in vivo

BABL/C female mice were divided into three groups (4 mice/group), control group was injected with glucose solution through the tail vein, and treatment groups (1 day group and 14 days group) were intravenously injected with HA-$FeWO_4$ (1 mM Fe/kg) and sacrificed at 1 and 14 days post injection, respectively. The bodyweight of all mice was measured every 2 days. The collected blood samples were tested to obtain the biochemical indicators. The histopathological changes of major organs (including heart, liver, spleen, lung and kidney) were obtained using H&E.

MRI/CT Dual-Modality Imaging in vivo

The 6 week old female BABL/C mice (average body weight: 18 g) were subcutaneously injected with 1×10^6 4T1 mouse breast cancer cells in 0.2 mL glucose solution on the left leg root. When the tumors grew to 0.8 cm^3, the mice were anaesthetized using a small animal ventilator with isoflurane (1.5%) and experienced MRI/CT imaging in vivo.

In vivo MRI of mice was performed on 3.0 T Prisma MR (Siemens, German) with a wrist coil. For each mouse, T2WI and T2* map were achieved both before and after intravenous injection of the HA-$FeWO_4$ nanoparticles (0.7 mM Fe/kg) and 5% glucose solution, respectively, at the time points of 5 min, 1, 2, 4, 6 and 12 h post-injection (T2WI: TE = 70 ms, TR = 3000 ms, matrix = 256×256, slice thickness = 1 mm, FOV = 120 mm, flip angle = 150°; T2* map: TE = 2.98 ms, TR = 293.0 ms, matrix = 256×256, slice thickness = 2 mm, FOV = 120 mm, flip angle = 60°). After the scanning, T2* values of the tumors were measured using the MRI post processing workstation.[46]

For in vivo tumor CT imaging, 50 μL of HA-$FeWO_4$ NPs (1.0 mM W/kg) and commercial iohexol agent (1.0 mM I/kg) were intratumorally injected into the 4T1 tumor-bearing mice anesthetized with isoflurane. CT images were obtained on IQon CT (Philips, Holland) and CT values of tumor were further measured according to the previous study.[48,49] The parameters of CT scanning were as follows: tube voltage 120 kV, tube current 60 mAs, matrix 512×512, slice thickness 0.8 mm.

Photothermal Experiments of HA-$FeWO_4$ in vitro and vivo

First, 1 mL of HA-$FeWO_4$ dispersion with a variety of concentrations (0, 25, 50, 100, 200 μg/mL) in a plastic centrifuge tube (1 mL), was irradiated for 5 min with an 808 nm laser (1.5 W/cm^2). The temperatures of the above solution during the irradiation were recorded with an FLIR thermal imaging camera, and the interval time of photographing was set to 10s. Furthermore, in order to evaluate in vitro photothermal cycle stability, repetitive irradiation with laser-on for 5 min

and then laser-off were performed. And then, 1 mL of HA-$FeWO_4$ NPs aqueous (200 μg/mL) was also irradiated for 5 min with an 808 nm laser (1.0 W/cm^2 and 2.0 W/cm^2). Real-time temperatures of the sample were monitored.

To explore the photothermal effect of cancer cell in vitro, 4T1 cells were cultured for 24 h and then treated with different concentrations of HA-$FeWO_4$ (0, 12.5, 25, 50, 100 μg/mL) for 1 h. Then, 4T1 cells were washed and irradiated with an 808 nm laser for 5 min (power density: 1.5 W/cm^2). Real-time temperatures of all wells were recorded by an FLIR A300 camera. After that, the cells were incubated for another 2 h and then the CCK-8 test was performed to assess the PTT efficacy of HA-$FeWO_4$ on 4T1 cells.

Furthermore, inhibition effect of tumor growth after PTT induced by HA-$FeWO_4$ was evaluated by measuring the sizes. Nine female BABL/C mice with 4T1 tumors were randomly categorized into 3 groups, including the laser, intravenous injection (200 μL, 10 mg/mL) + laser and intratumoral injection (100 μL, 10 mg/mL) + laser groups. After the injection of HA-$FeWO_4$, the intratumoral injection + laser group were irradiated immediately with an 808 nm laser for 10 min (power density: 1.5 W/cm^2). For the intravenous injection + laser group, tumors were irradiated using the same parameters after 6 h of injection. The laser group was only treated with an 808 nm laser under the same conditions. After PTT treatments, all mice were weighed and the sizes of tumors were recorded each other day. Tumor volumes and relative tumor volumes were calculated.

Results and Discussion

Characterization of HA-$FeWO_4$ NPs

The morphology and size of HA-$FeWO_4$ NPs were determined by TEM (Figure 1a), which showed a spherical-like morphology and a well-distributed particle size with a mean diameter of 91.4 nm (Figure S1). In addition, the crystal structure of HA-$FeWO_4$ NPs was tested by high-resolution TEM, a clear crystal lattice fringe of 0.37 nm was observed, which matched well with the (002) crystallographic plane of the wolframite-type monoclinic $FeWO_4$ (Figure 1b). Elemental dispersive spectrum (EDS) analysis showed the presence and distribution of Fe, W, O, C and N elements in the HA-$FeWO_4$ NPs (Figure S2). The quantification analysis of EDS demonstrated that the atomic ratio of Fe to W was close to 1:1, which was in consistent with the results of the elemental contents determined by ICP-OES. As shown in Figure 1c, the crystal structures of HA-$FeWO_4$ NPs matched with the standard JCPDS no. 71–2391, demonstrating the successful synthesis of $FeWO_4$. To further reveal the formation of HA-$FeWO_4$, FTIR spectra were obtained. As shown in Figure 1d, for HA or HA-$FeWO_4$, the peak at 3429 cm^{-1} was ascribed to the stretching vibration of -OH, and the symmetric and asymmetric stretching vibration of C=O (-COOH) at 1627 cm^{-1} and 1407 cm^{-1}, and the C-O vibration of

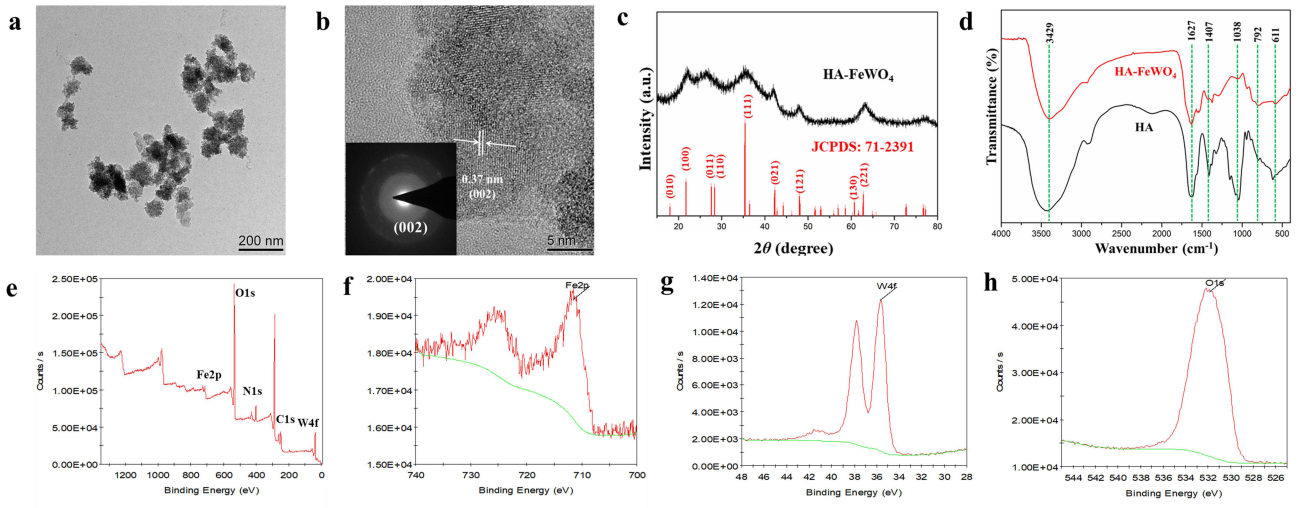

Figure 1 Characterization of HA-$FeWO_4$ NPs. (**a**) TEM images of HA-$FeWO_4$ NPs. (**b**) High resolution TEM images and mapping of HA-$FeWO_4$ NPs. (**c**) XRD pattern of HA-$FeWO_4$ NPs and the standard JCPDS (card no. 71–2391) file of $FeWO_4$. (**d**) FTIR spectra of HA-$FeWO_4$ NPs and HA. (**e**) XPS spectrum of HA-$FeWO_4$ NPs. (**f**) High-resolution XPS spectra of Fe 2p. (**g**) High-resolution XPS spectra of W 4f. (**h**) High-resolution XPS spectra of O 1s.

the carbohydrate chain at 1038 cm^{-1}, were all observed in the FTIR spectra of HA and HA-$FeWO_4$. Moreover, the formation of HA-$FeWO_4$ NPs was further identified by X-ray photoelectron spectra analysis (Figure 1e–h), the peaks at 35.67, 285.13, 400.07, 531.89 and 711.41 were assigned to the binding energies of W 4f, C 1s, N 1s, O1s and Fe 2p, respectively, which further verified the successful synthesis of HA-$FeWO_4$ NPs. Stability assay showed that HA-$FeWO_4$ possessed excellent dispersity without precipitating or aggregating in PBS, normal saline, RPMI-1640 and DMEM, demonstrating the good colloidal stability of HA-$FeWO_4$ (Figure S3).

Reflexivity and Hounsfield Unit (HU) Value Measurement

It's significant to evaluate the magnetic properties and X-ray attenuation of the HA-$FeWO_4$ NPs before their usage as MRI/CT dual-modality contrast agents. As shown in Figure 2a and b, T1 weighted image and T2WI showed an obvious concentration dependent contrast effect (brightening or darkening) with the longitudinal relativity value (r_1) of 0.6432 mM^{-1} s^{-1} and transverse relativity value (r_2) of 6.6382 mM^{-1} s^{-1}, respectively. Specially, the HA-$FeWO_4$ NPs exhibited strong visible T2WI blackening ability, which indicated the potential of HA-$FeWO_4$ in T2WI.

Furthermore, CT imaging of HA-$FeWO_4$ NPs was performed in solution as shown in Figure 2c and d. CT images of the HA-$FeWO_4$ solution showed a brightening trend with the increase in the concentration and the corresponding Hounsfield unit (HU) values increased linearly with the concentration of HA-$FeWO_4$ NPs. The results indicated that HA-$FeWO_4$ NPs displayed a good dispersion and excellent CT imaging ability. The linear slope of the HA-$FeWO_4$ NPs was 5.388 HU mM^{-1}, which was higher than the coefficient of iohexol (4.233 HU mM^{-1}) under the same conditions (Figure 2d). This indicated that HA-$FeWO_4$ NPs had an excellent X-ray absorption coefficient and a great potential in enhanced CT imaging.

Cytotoxicity Assessment

In order to investigate cytotoxicity, cell viability of MCF-10A and 4T1 cells in different concentrations of HA-$FeWO_4$ NPs was evaluated by CCK-8 test. As shown in Figure 3a, the HA-$FeWO_4$ NPs exhibited rather low toxicity toward MCF-10A and 4T1 cells whose cell viability remained above 80% in the range of 0–100 μg/mL of HA-$FeWO_4$ NPs. These results demonstrated that the HA-$FeWO_4$ possessed a good biocompatibility with no serious cytotoxicity in vitro, which encouraged us to further study the in vivo toxicity of HA-$FeWO_4$ NPs.

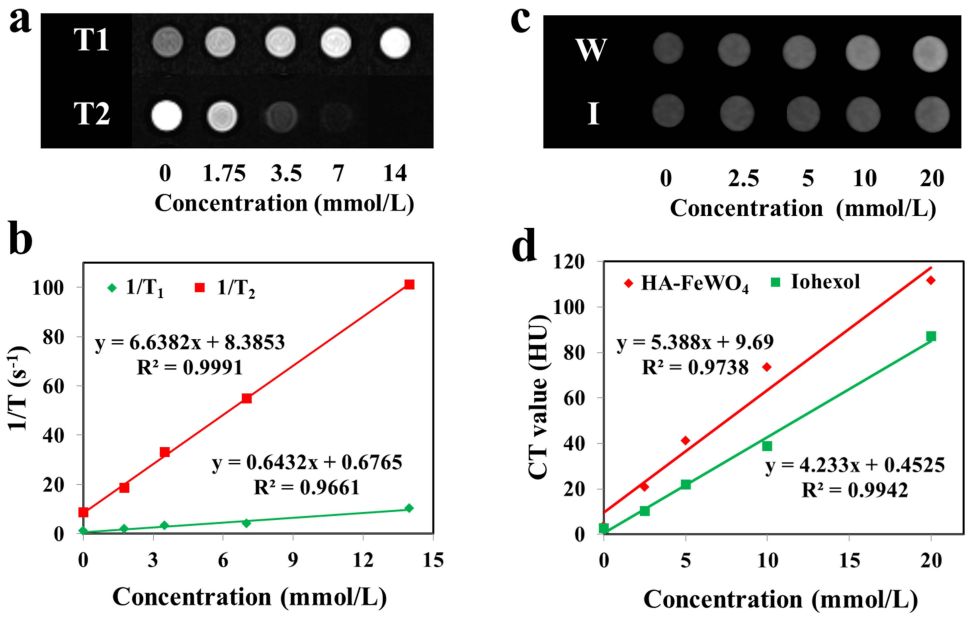

Figure 2 In vitro MRI and CT imaging performance. (**a**) T1- and T2- weighted images of HA-$FeWO_4$ NPs in different concentrations. (**b**) Relativities of HA-$FeWO_4$ NPs at different Fe concentrations (r_1 = 0.643 $mM^{-1}s^{-1}$, r_2 = 6.638 $mM^{-1}s^{-1}$). (**c**) In vitro CT imaging of iohexol and HA-$FeWO_4$ NPs in different concentration. (**d**) The CT values of the HA-$FeWO_4$ NPs and iohexol in different concentrations.

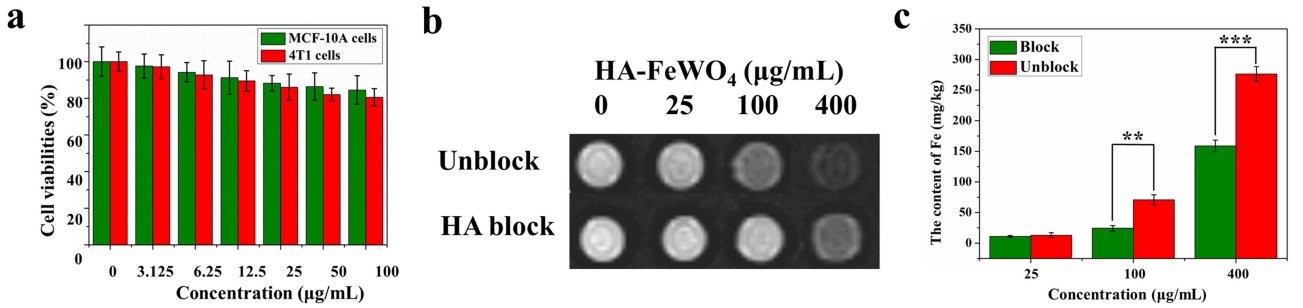

Figure 3 In vitro toxicity and targeting assay of HA-$FeWO_4$ NPs. (**a**) Cell viabilities of MCF-10A and 4T1 cells after incubation with different concentrations of HA-$FeWO_4$ NPs for 24 h. (**b**) T2-weighted MRI imaging results and (**c**) Fe contents of HA-blocked and unblocked cells treated with different concentrations of HA-$FeWO_4$ measured by ICP-OES. **P < 0.01, ***P < 0.001.

Vitro Targeted Assessment

In order to verify the targeting ability of HA-$FeWO_4$ NPs toward 4T1 cells, the receptor-blocking assay was performed. The T2WI results demonstrated that both the unblocked and HA blocked cells exhibited a gradual darkening effect with the increase in the concentration of HA-$FeWO_4$ (Figure 3b). However, the unblocked 4T1 cells possessed a more darkening image than HA-blocked cells at the same concentration of HA-$FeWO_4$. The ICP-OES results showed that HA-unblocked 4T1 cells internalized more HA-$FeWO_4$ NPs than the HA-blocked cells at the same concentration of HA-$FeWO_4$ (Figure 3c), which was consistent with the T2WI results. The results demonstrated that the good targeting ability and cellular imaging ability of HA-$FeWO_4$ NPs toward 4T1 cells made them promising candidates in 4T1 tumor imaging and treatment.

Hemolysis Assay

Hemolysis assay was carried out to assess the biocompatibility of HA-$FeWO_4$ NPs, where ultrapure water and PBS were used as positive and negative controls, respectively. As shown in Figure S4a, when HA-$FeWO_4$ NPs in different concentrations (50, 100, and 200 μg/mL) were exposed to the RBCs suspension, negligible hemolysis phenomenon was detected, which was similar to the negative PBS control. Furthermore, the hemolysis percentages of HA-$FeWO_4$ NPs were less than 2% in the tested concentration range, indicating the admirable hemocompatibility of the HA-$FeWO_4$ (Figure S4b).

Toxicity Assessment in vivo

For biochemical analysis in vivo, the liver function markers (aspartate aminotransferase, AST; alanine aminotransferase, ALT; alkaline phosphatase, ALP; albumin, ALB; total protein, TP; globulin, GLO; total bile acid, TBA) and kidney function markers (creatinine, Crea; Urea nitrogen, Urea) at 1st and 14th days post injection seemed to be normal compared with the control group, demonstrating that HA-$FeWO_4$ NPs had no obvious liver and kidney damage (Figure 4a). The body weights of the control group and HA-$FeWO_4$ NPs group kept similar increases, and no death or body-weight drop were observed in both groups (Figure 4b). H&E staining of major organs (heart, liver, spleen, lung, and kidney) showed that no obvious lesions, inflammation, hemorrhage, or necrosis were observed in these examined organs (Figure 5). These results demonstrated that the synthesized HA-$FeWO_4$ NPs were relatively safe and could be used for further biologic applications.

MRI/CT Dual-Modality Imaging in vivo

T2WI and T2* map of mice intravenously injected with HA-$FeWO_4$ at different time points were acquired to explore the MRI feasibility of HA-$FeWO_4$ for in vivo. Figure 6a showed the T2WI images of 4T1 tumor model before injection, 6 h and 12 h post-injection, respectively. The signal intensity of the tumor gradually decreased over time after the intravenous administration of the HA-$FeWO_4$ NPs. At about 6 h post-injection of HA-$FeWO_4$, the signal of the tumor site became the darkest and gradually brightened. Correspondingly, T2* values of the tumor descended in the first place, and then raised up 6 h after due to metabolic

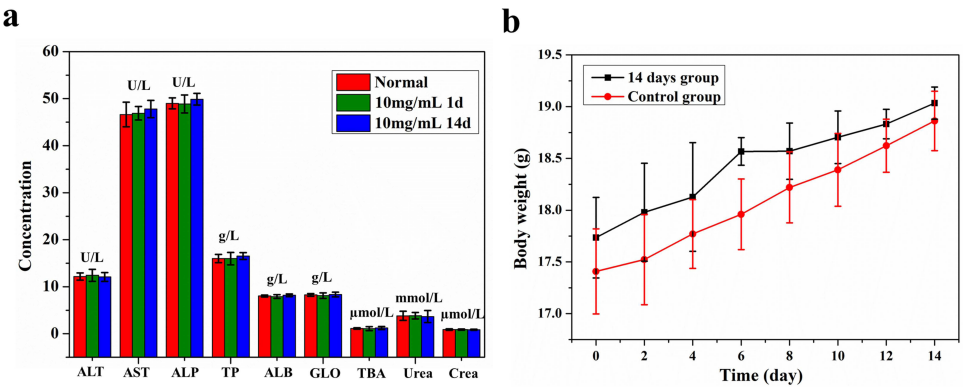

Figure 4 Toxicology evaluation of HA-$FeWO_4$ NPs. (**a**) Biochemical markers of mice at various time points (1st and 14th days) after intravenously administration of 200 μL HA-$FeWO_4$ NPs (1 mM Fe/kg). (**b**) The changes in body weight in different groups measured every 2 days.

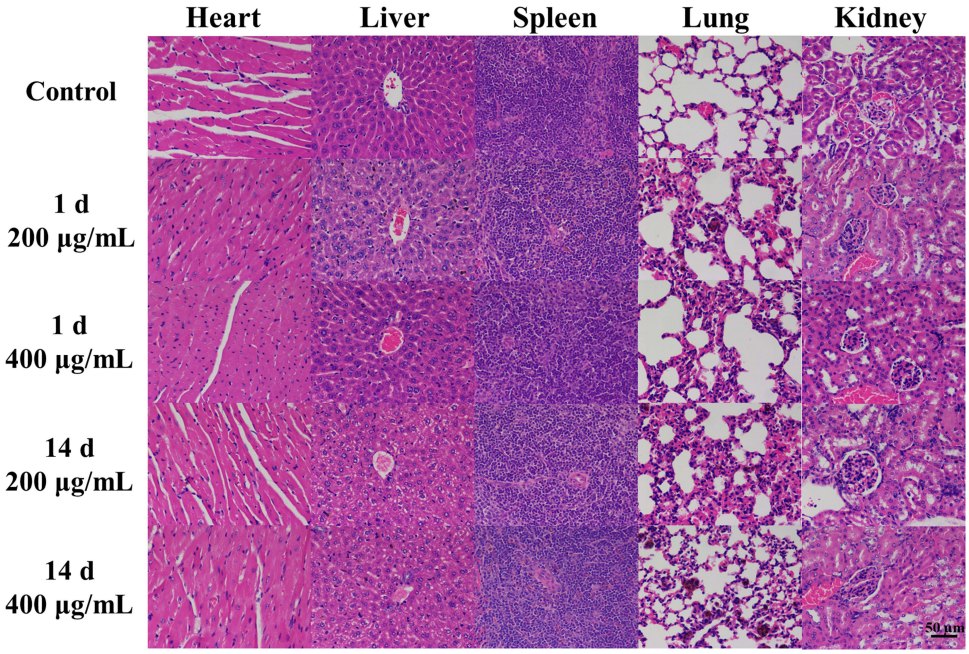

Figure 5 Haematoxylin and eosin (H&E) staining of important organs for normal mice at different time points after the injection of HA-$FeWO_4$ NPs and 5% glucose solution via the tail vein. Scale bar, 50 μm.

processes (Figure 6b). The excellent effect of negative control demonstrated active targeting of HA-$FeWO_4$ to cancer cells, which suggested that HA-$FeWO_4$ NPs had great potential to be efficient MRI contrast agents. For the control group, no obvious blackening effect of the tumors was observed.

Considering the outstanding X-ray attenuation property of W element, CT imaging of 4T1 tumor-bearing mice was also performed. As shown in Figure 6c and d, after HA-$FeWO_4$ NPs administration, the tumor site significantly brightened (205 HU) compared to the pre-injection (43.8 HU). However, tumor of the control group had no obvious brightening except for a slight enhancement. These results indicated that the HA-$FeWO_4$ NPs could be used as promising contrast agents for the MRI/CT dual-modal imaging.

The in vivo biodistribution of HA-$FeWO_4$ in different organs including heart, liver, spleen, lung, kidney and tumor was quantitatively measured by ICP-OES (Figure S5). It's obvious that the Fe element in important organs and tumor tissue after injection of HA-$FeWO_4$ was higher than that in the control group. Furthermore, the ICP-OES data showed the high accumulation of HA-$FeWO_4$ in the liver and spleen. Meanwhile, our result demonstrated the significant uptake in

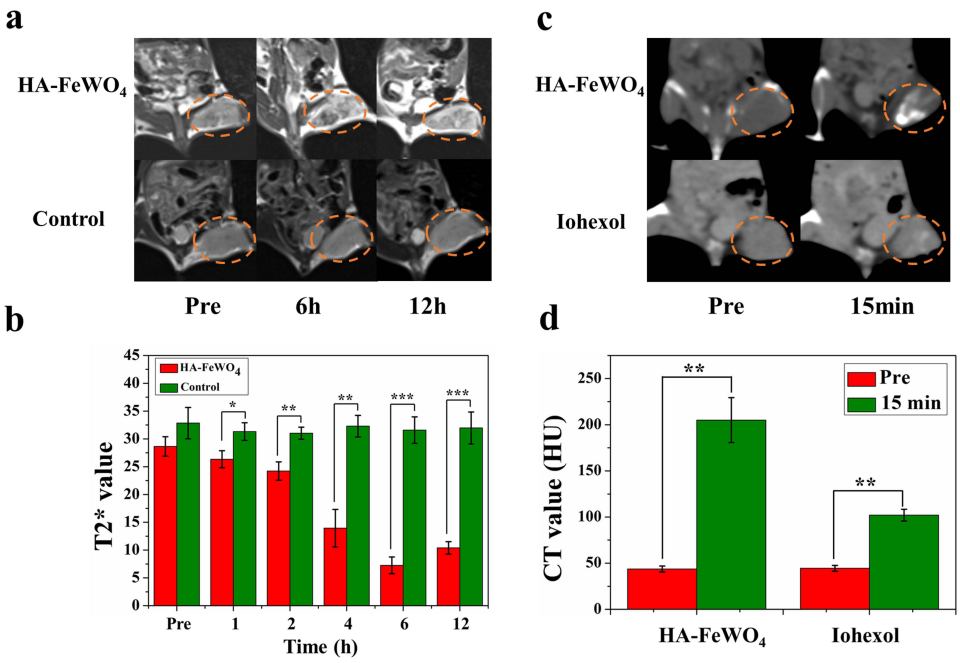

Figure 6 In vivo tumor-targeting imaging. (**a**) T2WI of 4T1 tumor-bearing mice before and after intravenous injection of HA-$FeWO_4$ NPs/glucose at different time points. (**b**) The T2* value of tumor at different time points before and after the injection. (**c**) In vivo CT images of 4T1 tumor-bearing mice before and after intratumoral administration. (**d**) CT value of tumor before and after the injection. Here, the tumor is marked in the Orange dashed circles. *P < 0.05, **P < 0.01, ***P < 0.001.

the tumor tissue of the mice after injection of HA-$FeWO_4$. The results confirmed that HA-$FeWO_4$ NPs could be well accumulated at the tumor site.

Photothermal Experiments of HA-$FeWO_4$ in vitro

Encouraged by the promising NIR-absorbance of the HA-$FeWO_4$ NPs, the photothermal capability of the nanoparticles in different concentration was detected (Figure 7a–c). It could be obviously seen that the temperatures of the HA-$FeWO_4$ solutions rapidly elevated with increasing concentration (0, 25, 50, 100, 200 μg/mL) and power density (1.0, 1.5, 2.0 W/cm^2). The temperature of HA-$FeWO_4$ solution in a lower concentration (25 μg/mL) increased 30.9°C and finally reached 49.5°C upon laser irradiation (power density: 1.5 W/cm^2), which could fully meet the demand of hyperthermia therapy of cancers. Then, the photothermal conversion efficiency of HA-$FeWO_4$ was calculated to be 72% using previously described protocol,[50] suggesting favourable photothermal conversion ability of HA-$FeWO_4$ NPs and great potential as PTT agent Figure S6). Moreover, photo-stability of HA-$FeWO_4$ NPs was studied by repetitive irradiation with laser-on for 5 min and then laser-off. The temperature-elevation ability of HA-$FeWO_4$ NPs showed no obvious change during the process, suggesting their excellent photo-stability (Figure 7d).

Next, the photothermal cytotoxicity of HA-$FeWO_4$ NPs was further investigated via the Live/Dead analysis in vitro, which was evaluated using calcein-AM and PI to stain the living and dead cells, respectively. As shown in Figure 8a, the number of dead cells in the laser treatment group increased with the increasing concentration of HA-$FeWO_4$. However, few dead cells were observed in the control group. Moreover, 4T1 cells incubated with various concentrations of were irradiated for 5 min. As shown in Figure 8b, the cell viability of 4T1 cells evidently decreased with the increase in the concentration of HA-$FeWO_4$ NPs upon irradiation, and about 87% of 4T1 cells were killed at the concentration of 100 μg/mLof HA-$FeWO_4$ NPs. These results suggested an effective hyperthermia therapy induced by HA-$FeWO_4$ NPs, which may become potential PTT agents for in vivo treatments.

Photothermal Experiments of HA-$FeWO_4$ in vivo

Photothermal experiments were performed to investigate the PTT effect of HA-$FeWO_4$ NPs in vivo. As showed in Figure 8c and d, the photothermal images of HA-$FeWO_4$-treated mice showed that the temperature of the tumor site risen

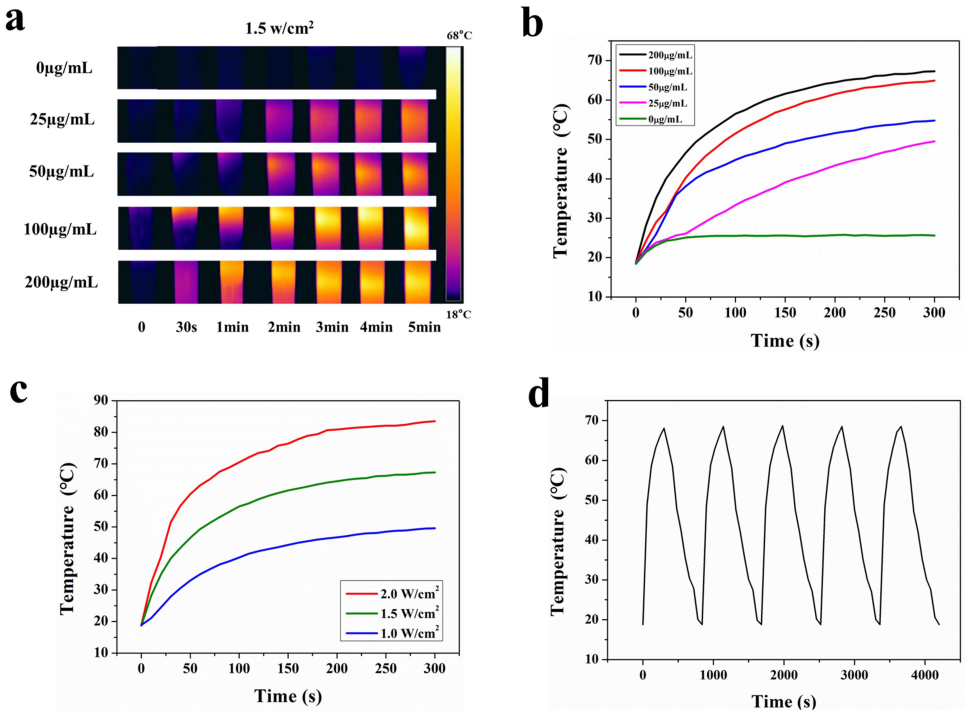

Figure 7 (**a**) Photothermal images of the HA-$FeWO_4$ NPs in solution. (**b**) Temperature change curves of HA-$FeWO_4$ NPs in different concentrations upon irradiation with 808 nm laser at 1.5 W/cm^2 for 5 min. (**c**) Temperature change curves of the HA-$FeWO_4$ NPs upon 5 min irradiation with 808 nm laser at various laser power densities. (**d**) Temperature change curves of the HA-$FeWO_4$ NPs solution during repetitive irradiation (5 times) with 5 min laser-on and then laser-off.

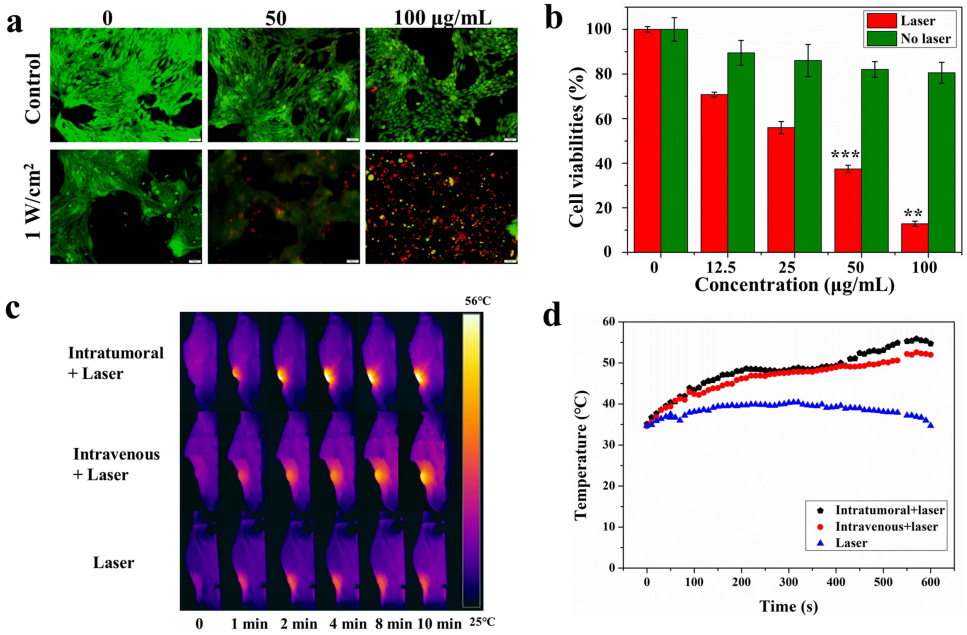

Figure 8 (**a**) Fluorescence images of 4T1 cells stained with calcein AM/PI after incubation with different concentrations of HA-$FeWO_4$ NPs under NIR laser irradiation or not. Scale bar, 50 μm. (**b**) Cell viabilities of 4T1 cells after incubation with different concentrations of HA-$FeWO_4$ NPs determined by CCK-8 assay with or without the laser treatment. (**c**) Infrared thermal images of the mice intratumorally or intravenously injected with the HA-$FeWO_4$ NPs and irradiated at different time intervals. (**d**) Real-time temperature elevation curves of the mice irradiated by laser-on for 10 min. **P < 0.01, ***P < 0.001.

rapidly from 34.6°C to 54.7°C (ΔT = 20.1°C) and 52.6°C (ΔT = 18°C) for the intratumoral injection + laser and intravenous injection + laser group, respectively, illustrating the efficient photothermal conversion of HA-$FeWO_4$ NPs in vivo. However, the temperature of the laser group only increased by ~5.8°C during the first 300 s, and then decreased

to 34.7°C gradually for the remaining time upon irradiation. The photothermal imaging of HA-$FeWO_4$ NPs further demonstrated that photon-to-thermal-conversion energy was accumulated and locally transferred at the tumor area. This favorable contrast in infrared thermal imaging should contribute to remote-control of tumor therapeutics.

The therapeutic effect of HA-$FeWO_4$ NPs on 4T1 tumor was assessed by measuring tumor sizes of mice every other day. As depicted in Figure 9a and b, the tumor grew rapidly without significant inhibitory effects in the laser group, and the average tumor size was about 3-fold larger than the original one. However, a significant inhibition effect was observed in the intratumoral injection + laser and intravenous injection + laser groups after 15 days of PTT treatment. Tumors even disappeared at 15th days in the intratumoral injection + laser and intravenous injection + laser groups, illustrating high PTT efficiency of HA-$FeWO_4$ NPs on 4T1 tumor. In addition, H&E staining of tumour slices from different groups at 24 h was shown in Figure S7. Severe cell death and damage, and significant infiltration of monocytes were observed in the laser treatment group, while no significant necrosis was found in the control group. As shown in Figure S8, the volume and weight of tumours in HA-$FeWO_4$ NPs treatment group became significantly smaller after PTT treatment compared with control group, and the tumor finally disappeared without relapse. Furthermore, all the mice survived from photothermal treatments, and their body weights increased gradually with a similar trend (Figure 9c), suggesting that no obvious biologic toxicity was induced by HA-$FeWO_4$ NPs. The results revealed the high PTT efficiency and favourable biosafety of HA-$FeWO_4$ NPs in vivo.

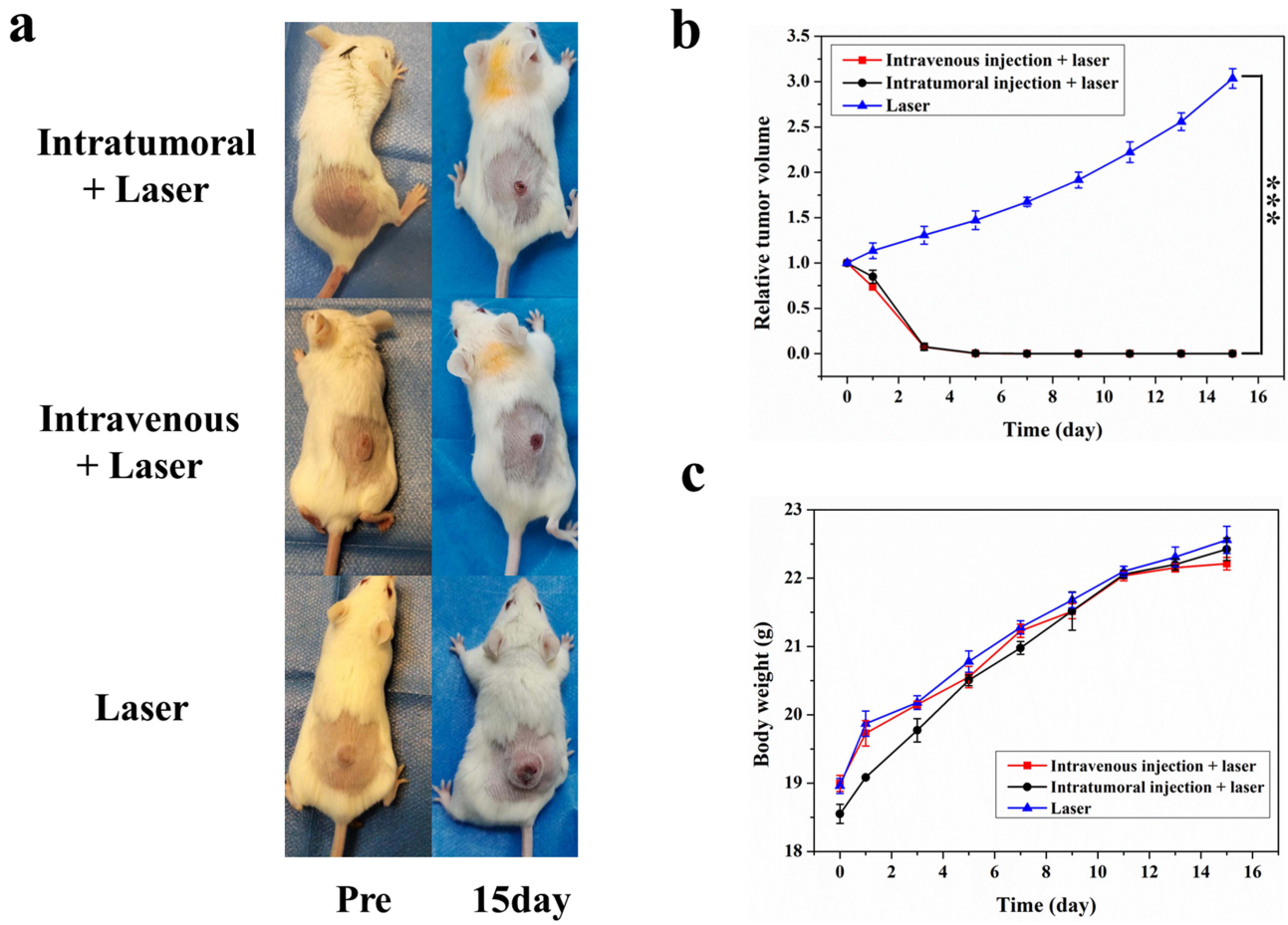

Figure 9 (**a**) Representative photos of mice in different groups after PTT for 15 days. Relative tumor volumes (**b**) and body weights (**c**) of the experimental mice versus a survival time. ***P < 0.001.

Discussion

Currently, multimodality imaging, which can utilize the inherent superiorities of different techniques to enable in vivo imaging with high specificity and high sensitivity, has been widely used in basic biomedical research and clinical diagnosis.[51] Correspondingly, many molecular probes capable of providing two or more imaging signals simultaneously have been synthetized to achieve multimodal imaging in vivo. Particularly, some activatable multimodal theranostic probes have also been reported to allow multimodal imaging-guided cancer therapy by integrating imaging components with PTT, photodynamic therapy (PDT), chemotherapy or immunotherapy.[52] Unfortunately, these types of multimodal theranostic probes are not applied in clinical practice due to multistep synthesis, batch-to-batch variation, nanoparticle aggregation, uncertain targeting ability or serious toxicity. Therefore, it remains a great challenge to develop novel efficient multimodal theranostic probes for precise diagnosis and treatment of disease.

Metal tungstates have some unique properties such as photoluminescence, catalysis, antiferromagnetism, and reduction activity, thus becoming novel materials for multiple applications, eg optical fibers, humidity sensors, photocatalysts, photoluminescence, scintillator materials and contrast agents in biological systems. To the best of our knowledge, some relevant investigations based on tungstates focused on single/multimodal imaging in vitro/vivo, including X-ray imaging, MRI imaging, optical imaging, photoacoustic and photothermal imaging. These nanoprobes provide superior contrast efficacy, which may bring more opportunities to the generation of novel contrast agents in biological systems.[13,14,53,54] Specially, $FeWO_4$ nanocomposites have been widely utilized due to their outstanding optical and electronic characteristics. However, only a few studies are related to their usage in biological fields.[25] Hence, it is significantly meaningful to verify the potential of $FeWO_4$ nanomaterial as contrast agents for tumor imaging and even imaging guided therapy.

In this study, we synthesized HA-$FeWO_4$ NPs as effective nanotheranostic agents for both MRI/CT dual-modality imaging and PTT in vitro and in vivo. The developed HA-$FeWO_4$ NPs exhibited excellent dispersion, good biocompatibility and lower cytotoxicity in vitro. Meanwhile, in vivo toxicity assessment further verified the excellent biosafety of HA-$FeWO_4$ NPs, indicating its great potential for in vivo application. Furthermore, in vitro and in vivo MRI/CT imaging indicated that HA-$FeWO_4$ could obtain better MRI/CT images compared with the control. More importantly, HA-$FeWO_4$ NPs showed outstanding photothermal efficiency and favorable tumor inhibitory activity by hyperthermia-killing of cancer cells. HA-$FeWO_4$ NPs could be served as versatile nanoplatform in terms of multimodal imaging and PTT, which may achieve precise diagnosis and treatment of disease.

There are certain limitations to our study. Considering the performance of primary toxicity evaluation and simple mice models in this study, we will further assess the long-term biotoxicity and multimodal imaging ability of HA-$FeWO_4$ in other animal models systematically, and assist the clinical research of HA-$FeWO_4$ in the future. Furthermore, despite our positive results in vitro and in vivo, long-time imaging and biodistribution at different time points should be assessed. Moreover, the MRI/CT imaging abilities of HA-$FeWO_4$ NPs were only tested in 4T1 tumor. Therefore, the imaging and therapeutic evaluation of other diseases/tissues will be conducted in the future.

Conclusion

In summary, novel $FeWO_4$ based dual-modality contrast agent HA-$FeWO_4$ NPs were developed in this work. HA-$FeWO_4$ NPs had superior stability, excellent biocompatibility, low toxicity, and effective cellular uptake, demonstrating their feasibility for in vivo applications. Furthermore, the HA-$FeWO_4$ NPs can be simultaneously served as T2WI and CT contrast agents for dual-modal imaging. More significantly, in vitro and in vivo study showed that the HA-$FeWO_4$ NPs had effective photothermal capacity, displaying high photothermal toxicity to 4T1 tumor without significant systemic toxicity in vivo, which was served as efficient PTT agent for imaging-guided cancer therapy. Our study suggests that HA-$FeWO_4$ NPs are expected to be promising candidates for clinical theranostic agents in the future.

Abbreviations

CT, computed tomography; MRI, magnetic resonance imaging; PTT, photothermal therapy; HA, Hyaluronic acid; RPMI-1640, Roswell Park Memorial Institute-1640; DMEM, dulbecco's minimum essential medium; FBS, fetal bovine serum;

DMSO, dimethyl sulfoxide; TEM, transmission Electron microscope; XRD, X-ray powder diffractometer; ICP-OES, inductively coupled plasma optical emission spectrometry; FTIR, Fourier transform infrared spectrometer; FOV, field of view; T2WI, T2 weighted imaging; TR, repetition time; TE, echo time; HRTEM, high resolution transmission electron microscopy.

Acknowledgments

We are grateful to the National Natural Science Foundation of China (No. 81903460), the Sichuan Province Science and Technology Program (No. 2023JDRC0098, 2022YFS0070 and 2022YFS0616), the Luzhou City Science and Technology Program (2023RQN179), the Technology Strategic Cooperation Project between Luzhou Municipal People's Government and Southwest Medical University (No. 2020LZXNYDJ42) and the National Training Program of Innovation and Entrepreneurship for Undergraduates (No.202310632066; S202310632212) for support of this research.

Author Contributions

All authors made a significant contribution to the work reported, whether that is in the conception, study design, execution, acquisition of data, analysis and interpretation, or in all these areas; took part in drafting, revising or critically reviewing the article; gave final approval of the version to be published; have agreed on the journal to which the article has been submitted; and agree to be accountable for all aspects of the work.

Disclosure

The authors report no conflicts of interest in this work.

References

1. Lee SY, Jeon SI, Jung S, Chung IJ, Ahn CH. Targeted multimodal imaging modalities. *Adv Drug Delivery Rev*. 2014;76:60–78. doi:10.1016/j.addr.2014.07.009
2. Liu M, Anderson RC, Lan XL, Conti PS, Chen K. Recent advances in the development of nanoparticles for multimodality imaging and therapy of cancer. *Med Res Rev*. 2020;40(3):909–930. doi:10.1002/med.21642
3. Ma H, Mu X, Tang Y, et al. Programmable multistage small-molecule nano-photosensitizer for multimodal imaging-guided photothermal therapy. *Acta Biomater*. 2023;157:408–416. doi:10.1016/j.actbio.2022.12.018
4. Feng W, Zhou XJ, Nie W, et al. Au/Polypyrrole@Fe_3O_4 Nanocomposites for MR/CT dual-modal imaging guided-photothermal therapy: an in vitro study. *ACS Appl Mater Interfaces*. 2015;7(7):4354–4367. doi:10.1021/am508837v
5. Ni DL, Zhang JW, Bu WB, et al. PEGylated $NaHoF_4$ nanoparticles as contrast agents for both X-ray computed tomography and ultra-high field magnetic resonance imaging. *Biomaterials*. 2016;76:218–225. doi:10.1016/j.biomaterials.2015.10.063
6. Zhou BQ, Xiong ZG, Zhu JZ, et al. PEGylated polyethylenimine-entrapped gold nanoparticles loaded with gadolinium for dual-mode CT/MR imaging applications. *Nanomedicine*. 2016;11(13):1639–1652. doi:10.2217/nnm-2016-0093
7. Liu YX, Guo QW, Zhu XJ, et al. Optimization of Prussian blue coated $NaDyF_4$: x% lu nanocomposites for multifunctional imaging-guided photothermal therapy. *Adv Funct Mater*. 2016;26(28):5120–5130. doi:10.1002/adfm.201601478
8. Branca M, Pelletier F, Cottin B, et al. Design of FeBi nanoparticles for imaging applications. *Faraday Discuss*. 2014;175:97–111. doi:10.1039/C4FD00105B
9. Chen Z, Qian LW, Zhu J, Yuan YP, Qian XF. Controlled synthesis of hierarchical Bi_2WO_6 microspheres with improved visible-light-driven photocatalytic activity. *Crystengcomm*. 2010;12(7):2100–2106. doi:10.1039/b921228k
10. Colon G, Lopez SM, Hidalgo MC, Navio JA. Sunlight highly photoactive Bi_2WO_6-TiO_2 heterostructures for rhodamine B degradation. *Chem Commun*. 2010;46(26):4809–4811. doi:10.1039/c0cc00058b
11. Thongtem S, Wannapop S, Thongtem T. Characterization of $CoWO_4$ nano-particles produced using the spray pyrolysis. *Ceram Int*. 2009;35(5):2087–2091. doi:10.1016/j.ceramint.2008.11.014
12. Zhang Q, Yao WT, Chen XY, et al. Nearly monodisperse tungstate MWO_4 microspheres (M = Pb, Ca): surfactant-assisted solution synthesis and optical properties. *Cryst Growth Des*. 2007;7(8):1423–1431. doi:10.1021/cg060827q
13. Dong K, Liu Z, Liu JH, et al. Biocompatible and high-performance amino acids-capped $MnWO_4$ nanocasting as a novel non-lanthanide contrast agent for X-ray computed tomography and T-1-weighted magnetic resonance imaging. *Nanoscale*. 2014;6(4):2211–2217. doi:10.1039/c3nr05455a
14. Wang MC, Liang YQ, Liao FL, et al. Iridium tungstate nanozyme-mediated hypoxic regulation and anti-inflammation for duplex imaging guided photothermal therapy of metastatic breast tumors. *ACS Appl Mater Interfaces*. 2022;14(51):56471–56482. doi:10.1021/acsami.2c14799
15. Zhou YX, Yao HB, Zhang Q, Gong JY, Liu SJ, Yu SH. Hierarchical $FeWO_4$ microcrystals: solvothermal synthesis and their photocatalytic and magnetic properties. *Inorganic Chemistry*. 2009;48(3):1082–1090. doi:10.1021/ic801806r
16. Zou Q, Tang RW, Zhao HX, Jiang JB, Li JL, Fu YY. Hyaluronic-acid-assisted facile synthesis of $mnwo_4$ single-nanoparticle for efficient trimodal imaging and liver renal structure display. *ACS Appl Nano Mater*. 2018;1(1):101–110. doi:10.1021/acsanm.7b00047
17. Shi H, Qi L, Ma J, Cheng H. Polymer-directed synthesis of penniform $BaWO_4$ nanostructures in reverse micelles. *J Am Chem Soc*. 2003;125(12):3450–3451. doi:10.1021/ja029958f

18. Jeong HY, Lee JH, Lee SY, Lee J, Cho SO. A transparent nano-polycrystalline $ZnWO_4$ thin-film scintillator for high-resolution X-ray imaging. *Acs Omega*. 2021;6(48):33224–33230. doi:10.1021/acsomega.1c05962
19. Rani BJ, Ravi G, Yuvakkumar R, et al. Bi_2WO_6 and $FeWO_4$ nanocatalysts for the electrochemical water oxidation process. *ACS Omega*. 2019;4(3):5241–5253. doi:10.1021/acsomega.8b03003
20. Hu X-L, Zhu Y-J. Morphology control of $PbWO_4$ nano- and microcrystals via a simple, seedless, and high-yield wet chemical route. *Langmuir*. 2004;20(4):1521–1523. doi:10.1021/la035578b
21. Yang RM, Fu CP, Fang JZ, et al. Hyaluronan-modified superparamagnetic iron oxide nanoparticles for bimodal breast cancer imaging and photothermal therapy. *Int j Nanomed*. 2017;12:197–206. doi:10.2147/IJN.S121249
22. Poovaragan S, Sundaram R, Magdalane CM, Kaviyarasu K, Maaza M. Photocatalytic activity and humidity sensor studies of magnetically reusable $FeWO_4$-WO_3 composite nanoparticles. *J Nanosci Nanotechnol*. 2019;19(2):859–866. doi:10.1166/jnn.2019.15565
23. Severo ED, Anchieta CG, Foletto VS, et al. Degradation of Amaranth azo dye in water by heterogeneous photo-Fenton process using $FeWO_4$ catalyst prepared by microwave irradiation. *Wat Sci Technol*. 2016;73(1):88–94. doi:10.2166/wst.2015.469
24. Gong C, Bai YJ, Feng J, et al. Enhanced electrochemical performance of $FeWO_4$ by coating nitrogen-doped carbon. *ACS Appl Mater Interfaces*. 2013;5(10):4209–4215. doi:10.1021/am400392t
25. Xiao ZY, Peng C, Jiang XH, et al. Polypyrrole-encapsulated iron tungstate nanocomposites: a versatile platform for multimodal tumor imaging and photothermal therapy. *Nanoscale*. 2016;8(26):12917–12928. doi:10.1039/C6NR03336A
26. Choi KY, Han HS, Lee ES, et al. Hyaluronic acid-based activatable nanomaterials for stimuli-responsive imaging and therapeutics: beyond CD44-mediated drug delivery. *Adv Mater*. 2019;31(34):e1803549. doi:10.1002/adma.201803549
27. Schmaus A, Sleeman JP. Hyaluronidase-1 expression promotes lung metastasis in syngeneic mouse tumor models without affecting accumulation of small hyaluronan oligosaccharides in tumor interstitial fluid. *Glycobiology*. 2015;25(3):258–268. doi:10.1093/glycob/cwu106
28. Stern R. Hyaluronidases in cancer biology. *Semi Cancer Biol*. 2008;18(4):275–280. doi:10.1016/j.semcancer.2008.03.017
29. Tan JX, Wang XY, Li HY, et al. HYAL1 overexpression is correlated with the malignant behavior of human breast cancer. *Intern J Can*. 2011;128(6):1303–1315. doi:10.1002/ijc.25460
30. Park KE, Noh YW, Kim A, Lim YT. Hyaluronic acid-coated nanoparticles for targeted photodynamic therapy of cancer guided by near-infrared and MR imaging. *Carbohydr Polym*. 2017;157:476–483. doi:10.1016/j.carbpol.2016.10.015
31. Soleymani M, Velashjerdi M, Shaterabadi Z, Barati A. One-pot preparation of hyaluronic acid-coated iron oxide nanoparticles for magnetic hyperthermia therapy and targeting CD44-overexpressing cancer cells. *Carbohydr Polym*. 2020;237:116130. doi:10.1016/j.carbpol.2020.116130
32. Souchek JJ, Wojtynek NE, Payne WM, et al. Hyaluronic acid formulation of near infrared fluorophores optimizes surgical imaging in a prostate tumor xenograft. *Acta Biomater*. 2018;75:323–333. doi:10.1016/j.actbio.2018.06.016
33. Du FY, Lou JM, Jiang R, et al. Hyaluronic acid-functionalized bismuth oxide nanoparticles for computed tomography imaging-guided radiotherapy of tumor. *Int j Nanomed*. 2017;12:5973–5992. doi:10.2147/IJN.S130455
34. Li JC, Hu Y, Yang J, et al. Hyaluronic acid-modified Fe_3O_4@Au core/shell nanostars for multimodal imaging and photothermal therapy of tumors. *Biomaterials*. 2015;38:10–21. doi:10.1016/j.biomaterials.2014.10.065
35. Pan YT, Ding YF, Han ZH, et al. Hyaluronic acid-based nanogels derived from multicomponent self-assembly for imaging-guided chemo-photodynamic cancer therapy. *Carbohydr Polym*. 2021;268:118257. doi:10.1016/j.carbpol.2021.118257
36. Zhao LP, Zhang X, Wang XX, Guan XW, Zhang WF, Ma JL. Recent advances in selective photothermal therapy of tumor. *J Nanobiotechnol*. 2021;19(1):335. doi:10.1186/s12951-021-01080-3
37. Lv F, Fan X, Liu D, Song F. Photothermal agents based on small organic fluorophores with intramolecular motion. *Acta Biomater*. 2022;149:16–29. doi:10.1016/j.actbio.2022.07.004
38. Duan S, Hu Y, Zhao Y, et al. Nanomaterials for photothermal cancer therapy. *RSC Adv*. 2023;13:14443–14460. doi:10.1039/D3RA02620E
39. Son J, Yi G, Yoo J, Park C, Koo H, Choi HS. Light-responsive nanomedicine for biophotonic imaging and targeted therapy. *Adv Drug Deliv Rev*. 2019;138:133–147. doi:10.1016/j.addr.2018.10.002
40. Yuan H, Fales AM, Vo-Dinh T. TAT peptide-functionalized gold nanostars: enhanced intracellular delivery and efficient NIR photothermal therapy using ultralow irradiance. *J Am Chem Soc*. 2012;134(28):11358–11361. doi:10.1021/ja304180y
41. Shi SG, Huang YZ, Chen XL, Weng J, Zheng NF. Optimization of surface coating on small Pd nanosheets for in vivo near-infrared photothermal therapy of tumor. *ACS Appl Mater Interfaces*. 2015;7(26):14369–14375. doi:10.1021/acsami.5b03106
42. Yong Y, Cheng XJ, Bao T, et al. Tungsten sulfide quantum dots as multifunctional nanotheranostics for in vivo dual-modal image-guided photothermal/radiotherapy synergistic therapy. *Acs Nano*. 2015;9(12):12451–12463. doi:10.1021/acsnano.5b05825
43. Cheng L, Yuan C, Shen SD, et al. Bottom-Up synthesis of metal-ion-doped ws_2 nanoflakes for cancer theranostics. *Acs Nano*. 2015;9(11):11090–11101. doi:10.1021/acsnano.5b04606
44. Cheng L, Liu JJ, Gu X, et al. PEGylated WS_2 nanosheets as a multifunctional theranostic agent for in vivo Dual-Modal CT/Photoacoustic imaging guided photothermal therapy. *Adv Mater*. 2014;26(12):1886–1893. doi:10.1002/adma.201304497
45. Liu JH, Han JG, Kang ZC, et al. In vivo near-infrared photothermal therapy and computed tomography imaging of cancer cells using novel tungsten-based theranostic probe. *Nanoscale*. 2014;6(11):5770–5776. doi:10.1039/c3nr06292a
46. Yan YL, Yang CM, Dai GD, et al. Folic acid-conjugated $CuFeSe_2$ Nanoparticles for Targeted T2-weighted magnetic resonance imaging and computed tomography of tumors in vivo. *Int j Nanomed*. 2021;16:6429–6440. doi:10.2147/IJN.S320277
47. Tan LF, Liu TL, Fu CH, et al. Hollow ZrO_2/PPy nanoplatform for improved drug delivery and real-time CT monitoring in synergistic photothermal-chemo cancer therapy. *J Mat Chem B*. 2016;4(5):859–866. doi:10.1039/C5TB02205C
48. Dai G, Zhang Y, Wang X, et al. Small-Molecule Bi-DOTA Complex for High-Performance CT and Spectral CT Bioimaging. *Front Oncol*. 2022;12:813955. doi:10.3389/fonc.2022.813955
49. Che X, Yang C, Pan L, et al. Achieving safe and high-performance gastrointestinal tract spectral CT imaging with small-molecule lanthanide complex. *Biomater Res*. 2023;27(1):119. doi:10.1186/s40824-023-00463-x
50. Jiang X, Zhang S, Ren F, et al. Ultrasmall Magnetic $CuFeSe_2$ ternary nanocrystals for multimodal imaging guided photothermal therapy of cancer. *ACS Nano*. 2017;11:5633–5645. doi:10.1021/acsnano.7b01032
51. Wang YQ, Hu YX, Ye DJ. Activatable multimodal probes for in vivo imaging and theranostics. *Angew Chem-Int Ed*. 2022;61(50):e202209512. doi:10.1002/anie.202209512

52. Huynh E, Leung BYC, Helfield BL, et al. In situ conversion of porphyrin microbubbles to nanoparticles for multimodality imaging. *Nature Nanotechnol*. 2015;10(4):325–332. doi:10.1038/nnano.2015.25
53. Guo T, Lin Y, Zhang WJ, et al. High-efficiency X-ray luminescence in Eu^{3+}-activated tungstate nanoprobes for optical imaging through energy transfer sensitization. *Nanoscale*. 2018;10(4):1607–1612. doi:10.1039/C7NR06405E
54. Jeong HY, Lim HS, Lee JH, Heo J, Kim HN, Cho SO. $ZnWO_4$ nanoparticle scintillators for high resolution X-ray imaging. *Nanomaterials*. 2020;10 (9):1721. doi:10.3390/nano10091721